Experiments on the MHD Effect on the Drainage of a LiPb Channel and Supporting Numerical Computations with the Level Set Method

Experiments on the MHD effect on the drainage of a LiPb channel and supporting numerical computations with the level set method

L. Candido[a]*, C. Alberghi[a], F. Papa[b], I. Ricapito[c], M. Utili[d], A. Venturini[d]

and M. Zucchetti[a,e]

[a]*ESSENTIAL Group, Politecnico di Torino, Corso Duca degli Abruzzi 24, 10129 Torino, Italy*

[b]*Sapienza University of Rome, Department of Astronautical, Electrical and Energy Engineering, Nuclear Section, Corso Vittorio Emanuele II 244, 00186 Roma, Italy*

[c]*Fusion for Energy (F4E), EU Commission Agency, Aix-en-Provence, Provence-Alpes-Côte d'Azur, France*

[d]*ENEA C. R. Brasimone, 40032 Camugnano (BO), Italy*

[e]*MIT, Massachusetts Institute of Technology, Cambridge (MA), US*

*corresponding author:

Luigi Candido

Department of Energy, Politecnico di Torino

Corso Duca degli Abruzzi, 24

10129 Torino - Italy

Tel: +39 011 090 4439

Mobile: +39 348 27 47 555

E-mail: luigi.candido@polito.it

Total number of pages: 24

Total number of figures: 11

Total number of tables: 7

Experiments on the MHD effect on the drainage of a LiPb channel and supporting numerical computations with the level set method

L. Candido, C. Alberghi, F. Papa, I. Ricapito, M. Utili, A. Venturini

and M. Zucchetti

To analyze the impact of the magneto-hydro-dynamic (MHD) effect on the fast draining of a LiPb channel (lithium-lead eutectic, 15.7 at. % Li) for a liquid metal fusion blanket such as the Water-Cooled Lithium-Lead (WCLL) of ITER or DEMO, an experimental campaign was carried out with the support of the experimental facility IELLLO (Integrated European Lead Lithium LOop), installed at ENEA Brasimone research center, Italy. The experiments were carried out by measuring the drainage time of the internal Permanent Magnet Pump (PMP) channel, normally used to circulate the LiPb in the loop, with and without the magnetic field. Moreover, this paper proposes a new numerical methodology to study the time delay induced by the MHD by using the commercial software COMSOL Multiphysics. In this way, it was possible to evaluate the LiPb fraction present at each time step in the computational domain and to estimate the time necessary to the complete drainage of the channel. The Level Set Method (LSM) was used to describe the transient behavior of the MHD flow under low-Rm approximation. The developed code was compared over the experimental results showing a good agreement, and it constitutes the first step in model validation as a possible application to ITER and DEMO. The experimental and numerical analyses performed in this work can be used as a benchmark case for MHD code development.

Keywords: MHD; level set method; ITER; DEMO

I. INTRODUCTION

There is a growing body of literature that recognizes the importance of the MHD effect related to liquid metals in fusion devices[1-6]. Of particular concern is the effect of -MHD on the increase of pressure drops and on corrosion-related issues due to the modification of the pure hydrodynamic velocity profile[7,8]. So far, however, very little attention has been paid to the time delay encountered in emergency draining procedures of a liquid metal channel.

Within this paper, a new numerical approach to the study of LiPb fast-draining under the action of a transverse magnetic field is presented. The model applies a conservative two-phase scheme of the Level Set Method (LSM) for incompressible flows to the MHD equations under low magnetic Reynolds approximation. The MHD analysis developed for this purpose compares a laminar model, a $k-\varepsilon$ standard turbulent model and a $k-\varepsilon$ turbulent model with damping terms accounting for the modifications induced by the Lorentz force. The numerical results were compared to the draining tests performed in IELLLO facility. In this way, it was possible to have a 3D computational tool able to study fast-draining procedures and to preliminarily validate the model over an experimental case study in view of possible applications to ITER and DEMO blankets.

The overall structure of this work is hereafter briefly described. Chapter II provides the description of the experimental tests performed on the drainage of the LiPb channel of the PMP. Chapter III presents an insight of the data analysis performed from the point of view of signal depuration and statistical treatment of the data. In Chapter IV, the numerical model is deeply explained, whereas Chapter V analyzes the main outcomes obtained from the finite element analysis, focusing on the comparison with the experimental results.

II. DESCRIPTION OF THE EXPERIMENT

The draining tests were performed in the lower part of IELLLO facility. IELLLO is a figure-of-eight facility in which LiPb circulates at a maximum mass flow rate of about 2.5 kg/s and can reach a maximum temperature of 550 °C in the hot side, while the cold side is always kept below 350 °C to protect the permanent magnet pump and the Coriolis flow meter. IELLLO was used in the past mainly to qualify instrumentation and components for flowing LiPb at relevant conditions for the HCLL TBS (Helium Cooled Lithium Lead)[9] and for the WCLL TBS (Ref. 10). With respect to the loop installed in 2008 (Ref. 11), IELLLO underwent a few modifications in 2015 and in 2018: in 2015, the original mechanical pump was substituted with a permanent magnet pump (PMP), while new instrumentation was added in 2018 (Ref. 9).

Experimental simulations of the emergency draining of IELLLO were performed with and without magnetic field applied on the PMP channel. The intensity of the magnetic field generated in the middle of the pump channel is about 0.7 T. The C-shaped pump channel (Figure 1) has a thickness of 2.5 mm, a width of 65 mm and a depth of 10 mm. The channel material is stainless steel type 1.4571 (316Ti).

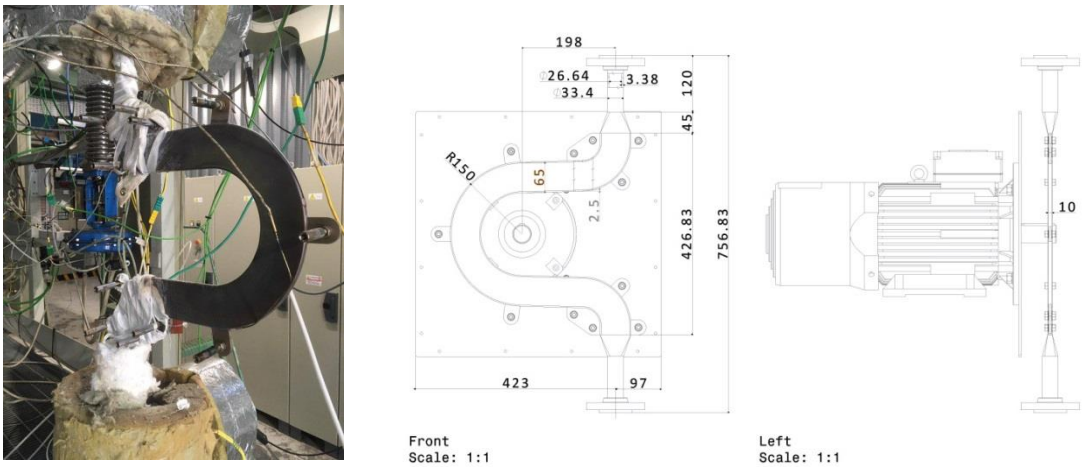

Figure 1. Picture and drawing of the pump channel without magnets.

The presence of the LiPb in the channel is revealed with the measure of the pressure with absolute pressure transducers installed at the inlet and at the outlet of the channel (vertical distance about 1006 mm), labelled as PT11 and PT12, respectively. The acquisition frequency of this instrument is 1 kHz, needed to accurately measure the draining time. The pressure trend at the top and at the bottom of the pumping channel (see Figure 2 and Figure 3) is decreasing as long as the LiPb is flowing; when there is no more LiPb at the level of the pressure transducer, the pressure signal becomes constant.

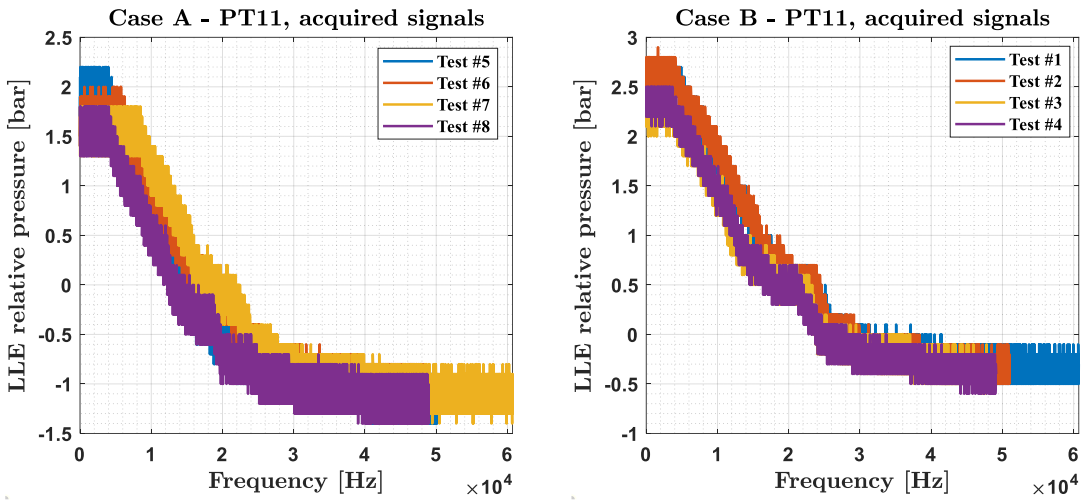

Figure 2. Acquired signals from PT11 pressure transducer for Case A (no magnets applied) and Case B (magnets applied).

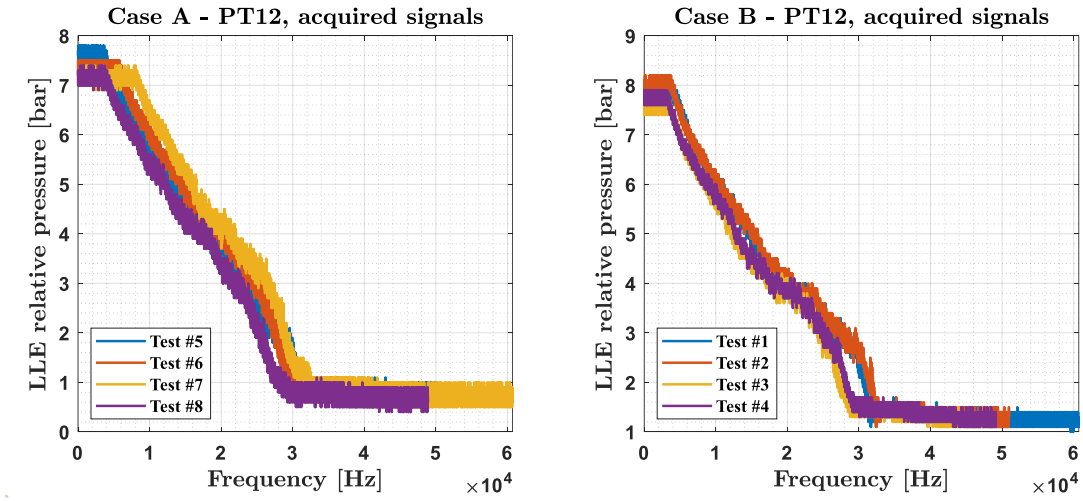

Figure 3. Acquired signals from PT12 pressure transducer for Case A (no magnets applied) and Case B (magnets applied).

III. DATA ANALYSIS

III.A. Signal analysis

In order to perform the calculation of the drainage time for each case, signals need to be depurated from the oscillating 50 Hz frequency due to power-line noise. To do so, a 21-points Savitzky-Golay (SG) filter[12] was applied to the rough signals; then, the obtained signals were resampled to remove small 50 Hz ripples. Finally, the signal was smoothed out. The results of the analyses are reported in TABLE I. The time delay represents the additional time due to the action of the magnetic field.

TABLE I. Times required to drain the pump channel.

	Case A (no magnets)	**Case B (with magnets)**	**Time delay**
Meas. 1 [s]	4.34	5.47	1.13
Meas. 2 [s]	4.89	6.42	1.53
Meas. 3 [s]	4.64	5.15	0.51
Meas. 4 [s]	4.69	5.47	0.78

III.B. Statistical analysis

The purpose of the statistical analysis is to have a tool for the comparison of the experimental results with the numerical simulations. A thorough analysis was conducted to assess the significance of the difference between the mean of the two groups. The descriptive statistics of the two groups are reported in TABLE II. Calculations were carried out with IBM SPSS Statistics[13] and RStudio[14].

TABLE II. Summary of descriptive statistics.

	Case A	Case B
Number of samples, N [-]	4	4
Mean value, $\bar{x}$ [s]	4.64	5.57
Standard error of the mean, $s_{\bar{x}}$	0.114	0.312
Median, m [s]	4.67	5.47
Standard deviation, s[s]	0.227	0.623
Variance, s^2 [s^2]	0.052	0.388
Skewness, γ_1 [-]	-0.639	0.930
Kurtosis, γ_2 [-]	1.50	1.99
Range, I [s]	0.55	1.50

For small sample sizes ($n < 30$), the sample distribution can be described by a Student t-distribution, provided that the population is normal. To test the normality, the Shapiro-Wilk (SW) test was selected since it is the most powerful[15-17]. The SW test algorithm adopted in this work (AS R94) was proposed by Royston[18-20]. The calculated p-value of the test was 0.797 and 0.199 for Case A and Case B, respectively. This means, that for a significance level $\alpha = 0.05$, the normality test fails to reject the null, allowing the populations of Case A and Case B to be described by normal distributions.

In order to choose the correct t-test, the assumption on the population variance was checked. Homoscedasticity was assessed through Levene's test[21] and O'Brien test[22,23]; the last one was chosen since it is more sensitive with respect to other tests (such as Brown-Forsythe test[24]) and minimizes type I and type II errors[25]. The p-value was 0.316 and 0.370 for Levene's and O'Brien's tests, respectively. For the given significance level $\alpha = 0.05$, both tests fail to reject the null Hence, homoscedasticity was assumed.

Once normality and homoscedasticity of the experimental data were assessed, two kinds of computations were performed. In the first one, the classical confidence intervals for the means of group A and B and for the time delay were calculated, along with the p-value of the test ($3.2 \cdot 10^{-5}$, $2.5 \cdot 10^{-4}$ and $1.6 \cdot 10^{-2}$, respectively). As shown in TABLE III, the calculation of confidence intervals (CI), lower confidence limit (LCL) and upper confidence limit (UCL) is affected by the remarkably low number of measurements for each group, obtaining too large confidence intervals. For this reason, a second calculation was carried out using the bootstrapping technique. Bootstrap methods[26] are based on random sampling with replacement. Among the different bootstrap methods, the bias-corrected and accelerated (BCa, Ref. 27) was selected. Mathematical details on CI derivation can be found in *Efron*[27] and *DiCiccio and Efron*[28].

It should be observed that BCa intervals are in general non-symmetric and influenced by the skewness of the sample distribution. A summary of the 95% CIs is given in TABLE III for both calculations. The BCa intervals are much narrower with respect to the no bootstrapping case and adjust for the bias due to the low number of samples. The relative variation of the confidence intervals amplitude, ΔCI, is remarkable, with a reduction up to 50%. As detailed in Chapter IV, COMSOL results are within both types of intervals.

TABLE III. Confidence intervals for no bootstrapping and BCa bootstrapping cases. Values in [s].

	LCL	UCL	CI	LCL	UCL	CI	Δ*CI*
	Without bootstrapping			With bootstrapping			
Case A	4.28	5.00	0.72	4.42	4.78	0.36	-50%
Case B	4.75	6.50	1.75	5.23	6.18	0.95	-46%

IV. FINITE ELEMENTS ANALYSIS (FEA)

In the frame of FEA, three cases were simulated, labelled as A, B and C, in order to describe the drainage of the LiPb channel of the permanent magnet pump. The first one represents an ordinary hydrodynamics analysis, without magnetic field. In case B, the MHD effect was considered. Finally, for case C the external magnetic field was set to 4 T. To verify the dependency of the draining time on the magnetic field, an intermediate case at 2 T was solved.

IV.A. The Level Set Method (LSM)

In an implicit interface representation, an interface is defined as the isocontour of some function. Level Set Methods (LSMs) are those numerical schemes which add dynamics to implicit surfaces[29]. These schemes may be not conservative, in the sense that surfaces and volumes are not preserved. However, the approach developed by *Olsson et al*[30,31] for a two-phase incompressible flow is conservative. The level set variable is represented by a smeared Heaviside function, which at the interface is equal to $\Phi = 0.5$:

$$H_{sm}(\Phi) = \begin{cases} 0, & \Phi < -\epsilon \\ \frac{1}{2} + \frac{\Phi}{2\epsilon} + \frac{1}{2\pi} sin\left(\frac{\pi\phi}{\epsilon}\right), & x - \epsilon \leq \Phi \leq \epsilon \\ 1, & \Phi > \epsilon \end{cases} \quad (1)$$

where ϵ [m] is half of the interface thickness Δx. For LiPb $\Phi = 0$, for argon $\Phi = 1$. The advection of the LSM function is described by the following partial differential equation:

$$\frac{\partial \Phi}{\partial t} + \vec{u} \cdot \nabla \Phi = \gamma \nabla \cdot \left[\varepsilon \nabla \Phi - \Phi(1 - \Phi) \frac{\nabla \Phi}{|\nabla \Phi|} \right] \quad (2)$$

where $\vec{u}$ [m s^{-1}] is the velocity field, γ [m s^{-1}] is called amount of reinitialization and has the function of avoiding ill-conditioning when numerically locating the interface. The parameter γ is normally assumed to be equal to the maximum velocity foreseen; to be conservative, we set $\gamma = 1$ [ms^{-1}]. Concerning the NS equations of momentum and mass conservation, they yield:

$$\rho \nabla \cdot \vec{u} = 0 \quad (3)$$

$$\rho \frac{\partial \vec{u}}{\partial t} + \rho(\vec{u} \cdot \nabla)\vec{u} = \nabla \cdot \left[-p\vec{\mathrm{I}} + \mu(\nabla \vec{u} + (\nabla \vec{u})^T) \right] + \vec{F}_g + \vec{F}_{sv} + \vec{F}_L \quad (4)$$

where p [Pa] is the pressure, $\vec{\mathrm{I}}$ is the identity matrix, $\vec{F}_g$ [Nm^{-3}] is the volume term accounting for the gravitational force, $\vec{F}_{sv}$ [Nm^{-3}] is the surface tension term and $\vec{F}_L$ [Nm^{-3}] is the term representing the volumetric Lorentz force due to MHD. It should be observed that $\rho = \rho_1 + (\rho_2 - \rho_1) \cdot \Phi$ and $\mu = \mu_1 + (\mu_2 - \mu_1) \cdot \Phi$ are the dimensionless density and viscosity varying smoothly on the interface, with ρ_1, ρ_2 and μ_1, μ_2 being the dimensionless densities and viscosities of the two fluids, respectively[30]. The fluid 2 is argon, since it was used to inert the loop; it can be assumed as incompressible since $Ma < 0.3$, where Ma is the Mach number. The reference properties were evaluated at the temperature $T = T_{ref} = 450$ [°C] which was the LiPb temperature during the experimental set-up. It can be demonstrated that Eq. (4) can be written in a dimensionless form by scaling the variables with opportune quantities. In this form, some

useful dimensionless number can be introduced: the Reynolds number $Re = \rho_{ref} u_0 L/\mu_{ref}$, the Froude number $Fr = u_0/\sqrt{Lg}$, and the Weber number $We = \rho_{ref} u_0^2 L/\sigma$. The characteristic length $L = 5 \cdot 10^{-3}$ [m] was chosen as half the height of the channel according to *Sano and Tamai*[32]. This is also in accordance with MHD, where the characteristic length is half the length in the direction of the external magnetic field.

IV.B. The MHD model

The Lorentz force term in Eq. (4) was evaluated with an independent MHD model. This choice was due to reduce the computational time and to avoid convergence issues. Moreover, the conservativeness of the LSM was never assessed in literature with MHD equations. Concerning the MHD, the low-Rm approximation for an incompressible fluid can be expressed by the following system of partial differential equations:

$$\rho \nabla \cdot \vec{u} = 0 \tag{5}$$

$$\rho \frac{\partial \vec{u}}{\partial t} + \rho(\vec{u} \cdot \nabla)\vec{u} = -\nabla p + \mu \nabla^2 \vec{u} + \vec{J} \times \vec{B}_0 \tag{6}$$

$$\nabla^2 \phi = \nabla \cdot (\vec{u} \times \vec{B}_0) \tag{7}$$

$$\vec{J} = \sigma_m \left(-\nabla \phi + \vec{u} \times \vec{B}_0\right) \tag{8}$$

Here, $Rm = u_0 L/\eta \ll 1$ is the magnetic Reynolds number, where η [$m^2 s^{-1}$] is the magnetic diffusivity, $\vec{J}$ [A m^{-2}] is the current density, B_0 [T] is the external magnetic field and ϕ [V] is the electric potential. In presence of turbulent flow, the unsteady motion can be described by Reynolds-Averaged Navier-Stokes (RANS) equations. They can be addressed using the $k - \varepsilon$ turbulent model, for which Eq. (6) becomes:

$$\rho \frac{\partial \vec{u}}{\partial t} + \rho(\vec{u} \cdot \nabla)\vec{u} = -\nabla p + (\mu + \mu_T)\nabla^2 \vec{u} + \vec{J} \times \vec{B}_0 \tag{9}$$

where $\mu_T = \rho C_\mu k^2/\varepsilon$ is the eddy viscosity, with constant $C_\mu = 0.09$. The two closure equations of the model are:

$$\rho(\vec{u}\cdot\nabla)k = \nabla\cdot\left[\left(\mu+\frac{\mu_t}{\sigma_k}\right)\nabla k\right]+P_k-\rho\varepsilon+S_k^L \tag{10}$$

$$\rho(\vec{u}\cdot\nabla)\varepsilon = \nabla\cdot\left[\left(\mu+\frac{\mu_t}{\sigma_\varepsilon}\right)\nabla\varepsilon\right]+C_{\varepsilon1}\frac{\varepsilon}{k}P_k-C_{\varepsilon2}\rho\frac{\varepsilon^2}{k}+S_\varepsilon^L \tag{11}$$

Here, P_k is a source term, σ_k, σ_ε, $C_{\varepsilon1}$ and $C_{\varepsilon2}$ are turbulent model parameters. S_k^L and S_ε^L are source terms due to the Lorentz force, and have been modelled by different authors[33-36]. For this work, the relations selected are the ones proposed by *Meng et al.*[35]:

$$S_k^L = -\sigma B^2 k e^{-C_1^M\sqrt{\frac{\sigma}{\rho}B^2\frac{\nu}{k}}} \tag{12}$$

$$S_\varepsilon^L = -\sigma B^2 \varepsilon e^{-C_1^M\sqrt{\frac{\sigma}{\rho}B^2\frac{\nu}{k}}} \tag{13}$$

where C_1^M is a constant with a value of 30. The system of MHD equations (5)-(8) can be made dimensionless, highlighting the interaction parameter $N = \sigma_m B_0^2 L/\rho_{ref}u_0$, and the Hartmann number, $Ha = \sqrt{N\cdot Re}$, whose square represents the ratio of Lorentz force to viscous force. For $Ha \gg 1$, the viscous forces are confined in boundary layers of thickness $O(Ha^{-1})$ and $O(Ha^{-1/2})$, respectively attached to walls perpendicular (Ha walls) or parallel (side walls) to the magnetic field. A summary of the dimensionless numbers introduced so far is given in TABLE IV. Even if the Reynolds number indicates a weak turbulent flow, since the resolution of a turbulent model for LSM is computationally expensive and considering the short duration of the transient, a laminar model was adopted. A scheme of resolution procedure of the coupled LSM and MHD models is in Figure 4.

TABLE IV. Dimensionless numbers used for the computation.

Name	Symbol	Definition	Significance	Value
Reynolds number	Re	u_0L/ν	Inertia/viscous forces	5986
Froude number	Fr	$U_0/\sqrt{gL}$	(Inertia forces/gravity force)$^{1/2}$	2.36
Weber number	We	$\rho U_0^2 L/\gamma$	(inertia forces/surf. tension force)	7.33
Inter. parameter	N	$\sigma_m B_0^2 L/\rho u_0$	Lorentz forces/inertia	0.28
Hartmann number	Ha	$(NRe)^{1/2}$	(Lorentz forces/viscous forces)$^{1/2}$	41.3
Magnetic Re number	Rm	u_0L/η	Advection/diffusion of B	$9.66\cdot10^{-4}$

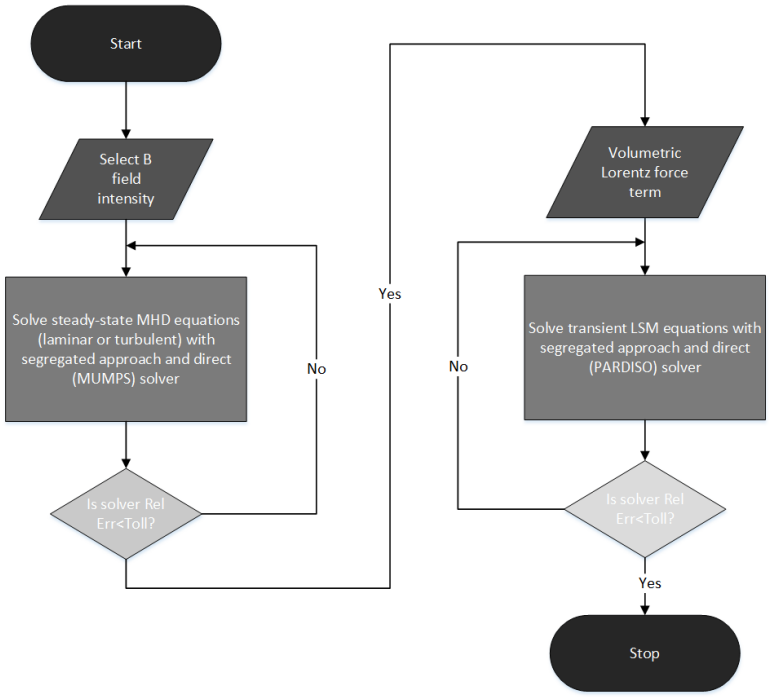

Figure 4. Numerical resolution scheme for the coupled MHD and LSM models.

IV.C. Geometry and Grid Independence Study

The 3D geometry of the pump channel as drawn in COMSOL is given in Figure 5, where half of the geometry is represented due to the symmetry with respect to xy plane. The connecting pipes to the pressure transducers have been also accounted in the computational domain.

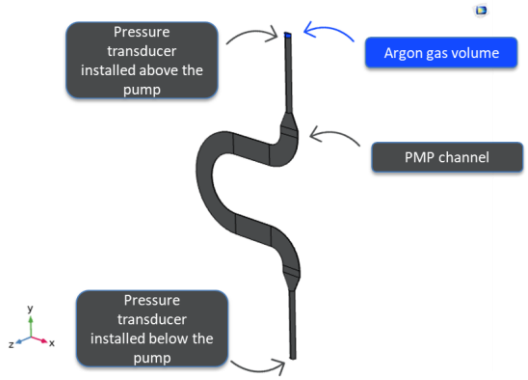

Figure 5. COMSOL 3D geometry adopted for the computations.

A grid convergence study for the case B was carried out according to the procedure exposed by *Roache et al.*[37] and *Celik et al.*[38] and suggested within the

ERCOFTAC best practice guidelines for industrial applications[39]. Three meshes, labelled M1, M2 and M3 were adopted, where M1 is the finest and M3 is the coarsest. A grid refinement factor, i.e. the ratio between the characteristic mesh element size between the finer to the coarser mesh, higher than 1.3 was adopted:

$$r = \frac{h_{coarse}}{h_{fine}} = \frac{\left(\frac{1}{N_{coarse}}\sum_i \Delta V_{i,coarse}\right)^{1/3}}{\left(\frac{1}{N_{fine}}\sum_i \Delta V_{i,fine}\right)^{1/3}} \quad (14)$$

This means, that the number of elements of the finer mesh has about twice the number of elements of the coarser mesh. A total of 8 variables, both local and global, were selected and reported in TABLE V, along with the Grid Convergence Indexes (GCIs). For the best mesh, M1, with respect to M2, the maximum Grid Convergence Index is 5.69% and the average one is 1.34%. Hence, M1 is used as the reference for all the computational cases.

TABLE V. Local and global variables adopted for the grid convergence study.

Label	Description	Type	GCI_{21} [%]	GCI_{32} [%]
ID1	Max velocity on volume	Local	2.97	1.14
ID2	Max on average core velocity on surface	Local	0.70	3.24
ID3	Average on max core velocity	Local	5.69	10.55
ID4	Max initial reciprocal interface distance	Local	0.11	0.53
ID5	LLE fraction	Global	0.0038	0.87
ID6	Average velocity on volume	Global	0.018	0.48
ID7	Average pressure on volume	Global	0.057	0.17
ID8	Average reciprocal interface distance	Global	1.20	4.93
		Average:	1.34	2.74

IV.D. Choice of the boundary conditions

Concerning the LSM, a wetted wall boundary condition was used along the pump channel, for which the extrapolated tangential velocity is zero at a distance β outside the wall; a suitable choice for this parameter, called slip length, is $\beta = h$, where h [m] is the mesh element size. The external boundary was described by a no flow condition applied to the level set variable Φ. A symmetry condition with respect to the xy plane was applied both to the velocity vector and to the level set variable. The inlet and outlet were set according to a prescribed inlet velocity and a zero relative pressure, respectively.

For the MHD models, a thin-wall BC for the electric potential was selected since the thickness of the pump channel is 0.5 [mm]. The wall conductance ratio, representing the ratio between wall conductance to fluid conductance, is defined as:

$$c_w = \frac{t_w \sigma_w}{L\sigma} \tag{15}$$

where t_w [m] is the thickness of the channel, σ_w [Sm^{-1}] is the electrical conductivity of the steel and σ [Sm^{-1}] is the electrical conductivity of lithium-lead. Here, we have $c_w = 3.25$. Even in this case, a symmetry condition for the currents was applied.

As far as the inflow characteristic velocity u_0 is concerned, the whole drainage process was considered. In fact, the presence of valves, elbows, roughness of the pipes, tees, flow meters and so on modify the LiPb velocity profile. For this reason, a separate COMSOL 1D hydraulic model of the entire facility was carried out in steady-state conditions, providing an inlet velocity $u_0 = 0.37$ [$\mathrm{m\,s}^{-1}$]. This study was solved adopting Churchill's equation for the friction factor[40]. The main input data are reported in TABLE VI, whereas details on the geometry of the loop are reported in (Ref. 9-11).

TABLE VI. Summary of the main input parameters for the inlet PMP velocity study.

Parameter	Symbol	Value
Operative temperature	T_{op}	450 [°C]
Pipes internal diameter	d_{int}	26.645 [mm]
Surface roughness	ε_{pipe}	$5 \cdot 10^{-5}$ [m]
Inlet pressure LiPb	p_{in}	1 [atm]
Outlet pressure LiPb	p_{out}	1 [atm]
Height of air cooler	h_{ac}	180 [mm]
Bend (90° standard elbow)	$K_{f,el}$	0.9 [−]
Tee junctions	$K_{f,T,main}$	0.4 [−]
	$K_{f,T,side}$	1.2 [−]
Valve PV01 (upper branch)	$K_{f,PV01}$	15.03 [−]
Valve PV04 (lower branch)	$K_{f,PV04}$	15.03 [−]
Δp Vortex flow meter	Δp_{fm}	0.13 [bar]

V. RESULTS AND DISCUSSION

As already mentioned, the objective of this work is to have a computational tool able to evaluate the impact of the time delay induced by the presence of an external magnetic field. To do this, the level set method was applied to the Navier-Stokes equations of continuity and momentum conservation; to take into account the MHD effect, a separate model of the central part of the pump (on which the magnetic field acts) was developed, evaluating the average effect to be used as volumetric force in the momentum equation.

The MHD effect on the velocity profile is displayed in Figure 6 for different models adopted. It can be seen that typical velocity jets are encountered at the channel sides and are overestimated by the laminar assumption. This effect is smoothed out when considering a turbulent model; the damping effect is negligible due to the low value of Ha. However, no significant differences on the average volumetric force were observed: 114.5 kN m^{-3} for the laminar case, 114.6 kN m^{-3} for the turbulent cases.

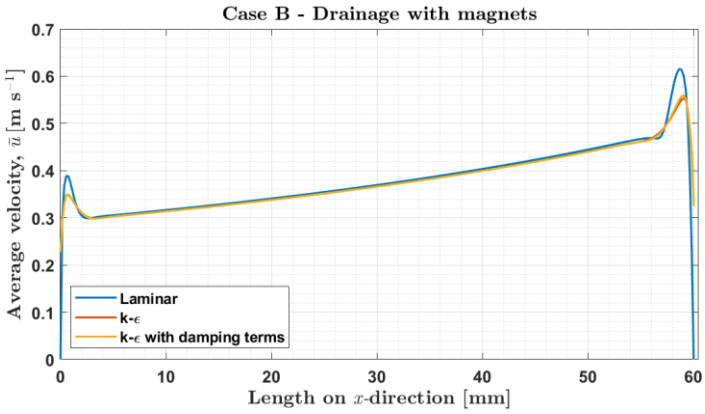

Figure 6. MHD velocity profile for Case B at the centre of the pumping channel for the different models developed (laminar, turbulent, turbulent with damping terms).

The drainage time was evaluated for both Case A and Case B, for which $t_A =$ 4.44 s and $t_B = 5.89$ s. Figure 7 compares the LiPb volume fraction χ_{LiPb} as a function

of the time. The case with the pump magnets switched on causes a delay in the time required for the 99.9% draining of the channel equal to $\Delta t_{BA} = 1.48$ s.

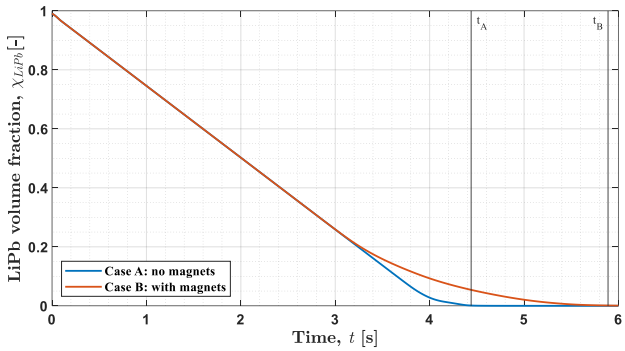

Figure 7. Drainage time evolution for Case A and Case B.

A graphical representation of the CIs for the case without and with bootstrapping, along with the normal distribution of the populations, is displayed in Figure 8. The populations for BCa cases are $\mathcal{N}(\mu_{BCa}, \sigma_{BCa})$ distributed. COMSOL results, depicted with an orange line, fall in the 95% CI for both interval evaluations.

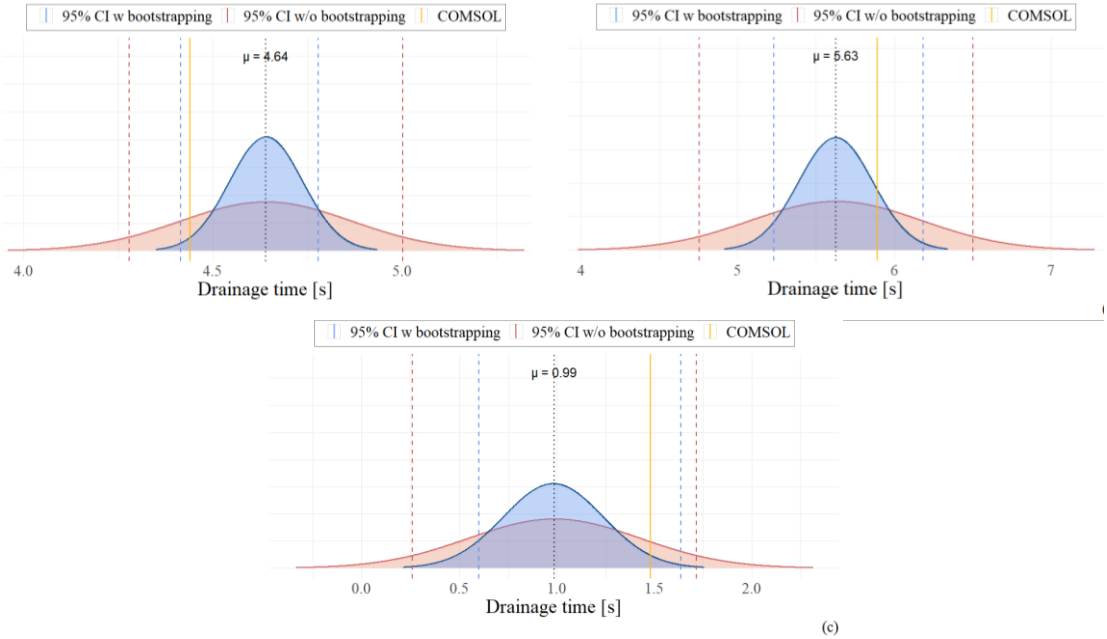

Figure 8. Comparison between CIs with no bootstrapping and with BCa bootstrapping.

To have representative values of the magnetic field encountered in ITER and DEMO operations, a numerical simulation with $B_0 = 4$ T is carried out. The results,

shown in Figure 9 and Figure 10. As for Case B, no particular differences were observed for the different models, with a difference less than 0.8%.

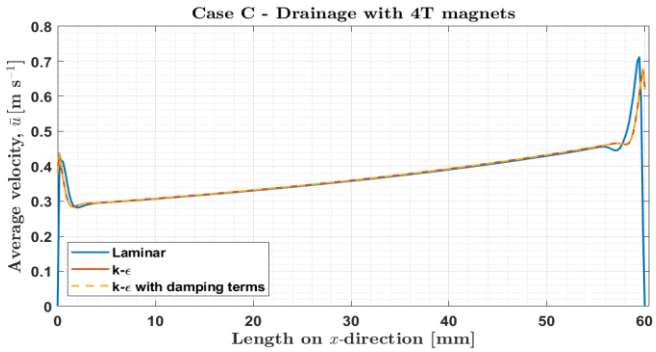

Figure 9. MHD velocity profile for Case C at the centre of the pumping channel for the different models developed (laminar, turbulent, turbulent with damping terms).

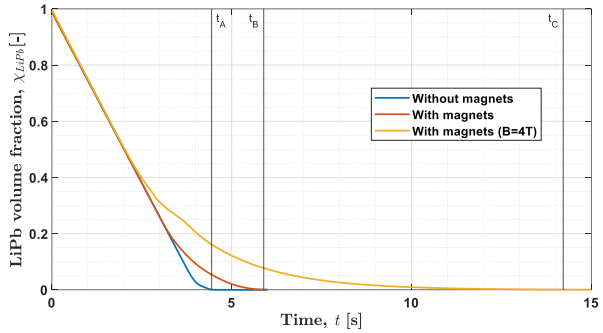

Figure 10. Drainage time evolution for Case A, Case B and Case C.

For Case C, $Ha = 236$, i.e. about six times higher than Case B; this results into a drainage time $t_C = 14.2$ s, hence a time about three times higher than Case A, causing a time delay $\Delta t_{CA} = t_C - t_A = 9.78$ s. A summary of the results for Case A, Case B and Case C is reported in TABLE VII.

TABLE VII. Summary of the COMSOL results for Case A, B and C.

	Symbol	Value	Units
Draining time, Case A	t_A	4.44	s
Draining time, Case B	t_B	5.89	s
Draining time, Case C	t_C	14.2	s
Time delay, Case B w.r.t. Case A	Δt_{BA}	1.48	s
Time delay, Case C w.r.t. Case A	Δt_{CA}	9.78	s

It is possible to define the proper time, $t^* = L/u_0$, as the time needed for a particle of fluid to travel a distance equal to the characteristic length of the channel L. This time

depends on the geometry of the channel once the boundary conditions of the problem are fixed. By applying Buckingham's Π theorem to Eqs. (3)-(4) a relationship between the different variables involved can be derived. In particular, it is possible to write:

$$t/t^* = f(N, Re^{-1}, Fr^{-2}, We^{-1}) \tag{16}$$

From Eq. (16) it can be concluded that once the geometry, the fluid properties and the boundary conditions of the problem are fixed, the drainage time is expected to increase as the square of the external magnetic field flux density; in other words, $t = f(B_0^2)$. The correlation:

$$t = 4.44 + 1.584 \cdot B_0 + 0.2124 \cdot B_0^2 \tag{17}$$

is optimal in the sense of the least-squares for the range $[0 - 4\ \mathrm{T}]$ and clearly shows the relationship between the drainage time and the square of the external magnetic field, keeping fixed all the other parameters. This correlation was obtained solving the case $B_0 = 2$ T. It has to be noted that the correlation is based on numerical simulations only. In Figure 11, Eq. (17) is reported along with its 95% confidence intervals; the COMSOL simulation results and the experimental values are also reported.

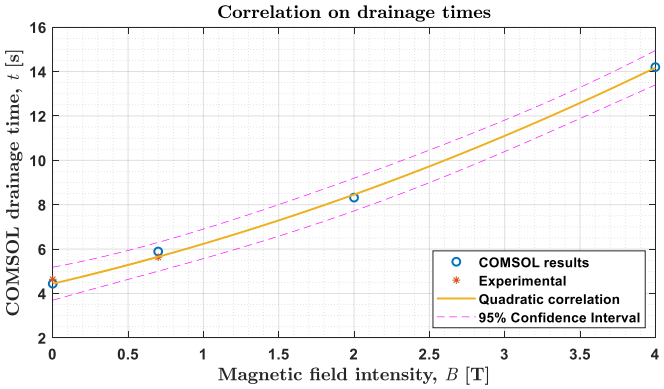

Figure 11. Correlation on drainage time as predicted by the four set of simulations Case A, Case B, Case C and $B_0 = 2$ T.

VI. CONCLUSIONS

Within this work, a new numerical model developed with the level set method for the study of fast draining of a LiPb channel under transverse magnetic field was presented. The model was preliminarily validated over a set of experiments carried out on the pumping channel of the PMP installed in IELLLO facility. In this way, the first step to validate the 3D model in view of ITER and DEMO applications was performed. The model can be easily adapted to different geometries representative of liquid metal breeding blankets and can be used as a benchmark case for MHD code development.

From the viewpoint of the experimental campaign, the delay induced by the presence of an external magnetic field on the drainage time of the PMP channel was measured. The pure hydrodynamics case, i.e. with the magnets removed from the permanent magnet pump, was labelled as Case A, whereas the case with the effect of the magnetic field was labelled as Case B. The data from IELLLO experiments were obtained by means of two pressure transducers installed above and below the pumping channel. The 1 kHz acquired signals were depurated from the 50 Hz power-line noise in order to have highly precise values in terms of drainage times. A statistical analysis was performed deriving the confidence intervals able to guarantee a $\pm 2\sigma$ precision. The calculation of the CIs was carried out with the standard t-test for independent samples and with the bias-corrected and accelerated bootstrapping method. By doing so, the CIs amplitude were consistently reduced up to 50%.

Afterwards, the level set method was introduced and a solution algorithm to take into account the MHD effect was presented. To derive the inlet lithium-lead velocity, a separate model able to describe all the piping involved, considering elbows, flow meters, tees, valves and so on was developed. From the steady state solution of this model, it was possible to evaluate the inlet velocity of lithium-lead and then to solve the LS/MHD

models. In this context, it has to be observed that the MHD effect was represented in the LSM model with an average volumetric force term proportional to the Lorentz force acting on the LiPb. Three different MHD models were developed: a laminar model a standard $k-\varepsilon$ turbulent model and a modified $k-\varepsilon$ model which takes into account some corrective terms due to the Lorentz force. The solution of these models showed that in terms of average volumetric force no particular differences were appreciable. Finally, the draining of the pumping channel was simulated through the dynamic motion of the interface separating the lithium-lead alloy and the gas phase.

The results showed a remarkable agreement between the experiments and the simulations. In particular, for Case A, Case B and for the time delay, the numerical results are statistically correct at a significance level $\alpha = 0.05$ for both the evaluations without and with bootstrapping. The time delay observed during the experiments was due to the dragging action exerted by the magnetic field on the lithium-lead alloy, especially in the final part of the transient. Furthermore, a new computational case, labelled as Case C, was developed. This case, characterized by an external magnetic field equal to 4 T, was developed in order to have a representation of the time delay which could be encountered in ITER and DEMO environments. For this case, the estimated delay was 9.78 s with respect to the pure hydrodynamics case. The time increase is due to a higher dragging force, which starts its action not only in the final part of the transient (with much longer times than expected with respect to Case B) but also in the central part of the transient, corresponding to the zone of the magnets. From a dimensionless analysis, it was evident that the drainage time and the time delay– fixed the geometry, the fluids properties and the boundary conditions of the problem – must increase as the square of the magnetic field.

REFERENCES

1 S. SMOLENTSEV et al., "MHD thermofluid issues of liquid-metal blankets: phenomena and advances," *Fusion Engineering and Design*, **85**, *7-9*, 1196-1205 (2010).

2 L. BÜHLER and C. MISTRANGELO, "MHD flow and heat transfer in model geometries for WCLL blankets," *Fusion Engineering and Design*, **124**, 919-923 (2017).

3 C. MISTRANGELO et al., "Three-dimensional magneto convective flows in geometries relevant for DCLL blankets," *Fusion Engineering and Design*, **159**, 111686 (2020).

4 A. TASSONE et al., "Influence of PbLi hydraulic path and integration layout on MHD pressure losses," *Fusion Engineering and Design*, **155**, 111517 (2020).

5 S. SAHU and R. BHATTACHARYAY, "Validation of COMSOL code for analyzing liquid metal magnetohydrodynamic flow," *Fusion Engineering and Design*, **127**, 151-159 (2018).

6 C. ALBERGHI et al., "Magneto-convective effect on tritium transport at breeder unit level for the WCLL breeding blanket of DEMO," *Fusion Engineering and Design*, **160**, 111996 (2020).

7 A. TASSONE et al., "MHD pressure drop estimate for the WCLL in-magnet PbLi loop," *Fusion Engineering and Design*, **160**, 111830 (2020).

8 L. BÜHLER et al., "Experimental investigation of liquid metal MHD flow entering a flow channel insert", *Fusion Engineering and Design*, **154**, 111484 (2020).

9 A. VENTURINI et al., "Experimental Qualification of New Instrumentation for Lead-Lithium Eutectic in IELLLO Facility," *Fusion Engineering and Design*, **156**, 111683 (2020).

10 A. VENTURINI et al., "Experimental and RELAP5-3D results on IELLLO (Integrated European Lead Lithium LOop) operation," *Fusion Engineering and Design*, **123**, 143–147 (2017).

11 M. UTILI et al., "The European breeding blanket test facility: an integrated design to test European helium cooled TBMs in view of ITER," *Fusion Engineering and Design*, **84**, *7-11*, 1881–1886 (2009).

12 A. SAVITZKY and M. GOLAY, "Smoothing and Differentiation of Data by Simplified Least Squares Procedure," *Analytical Chemistry*, **36**, 1627–1639 (1964).

13 IBM SPSS Software v. 26.0: https://www.ibm.com/analytics/spss-statistics-software (current as of Nov. 1, 2020).

14 RStudio Desktop v. 1.3: https://rstudio.com/ (current as of Nov. 1, 2020).

15 S. S. SHAPIRO and M. B. WILK, "An analysis of variance test for normality (complete samples)," *Biometrika*, **52**, 591–611 (1965).

16 S. S. SHAPIRO, and R. S. FRANCIA, “An approximate analysis of variance test for normality,” *Journal of the American Statistical Association*, **67**, 215–216 (1972).

17 N. MOHD RAZALI and Y. BEE WAH, “Power comparisons of Shapiro-Wilk, Kolmogorov-Smirnov, Lilliefors and Anderson-Darling tests,” *Journal of Statistical Modeling and Analytics,* **2**, 21–33 (2011).

18 J. P. ROYSTON, “Algorithm AS 177: Expected Normal Order Statistics (Exact and Approximate),” *Journal of the Royal Statistical Society, Series C (Applied Statistics),* **31**, 161–165 (1982).

19 J. P. ROYSTON, “Algorithm AS 181: The W Test for Normality,” *Journal of the Royal Statistical Society, Series C (Applied Statistics)*, **31**, 176–180 (1982).

20 J. P. ROYSTON, “A Remark on Algorithm AS 181: The W-test for Normality,” *Journal of the Royal Statistical Society, Series C (Applied Statistics)*, **44**, 547–551 (1995).

21 H. LEVENE, “Robust Tests for the Equality of Variances,” in *Contributions to Probability and Statistics: Essays in Honor of Harold Hotelling* (ed. Olkin, I.) 278–292 (Stanford University Press, 1960).

22 R. G. O’BRIEN, “A general ANOVA method for robust tests of additive models for variances,” *Journal of the American Statistical Association*, **74**, 877–880 (1979).

23 R. G. O’BRIEN, “A simple test for variance effects in experimental designs,” *Psychological Bullettin*, **89**, 570–574 (1981).

24 M. B. BROWN and A. B. FORSYTHE, “Robust tests for the equality of variances,” *Journal of the American Statistical Association*, **69**, 364–367 (1974).

25 H. ABDI, “O’Brien Test for Homogeneity of Variance,” in *Encyclopedia of Measurement and Statistics*, 1–9 (2007).

26 B. EFRON, “Bootstrap methods: another look at the jackknife,” *Annals of Statistics*, **14**, 590–606 (1986).

27 B. EFRON, “Better Bootstrap Confidence Intervals,” *Journal of the American Statistical Association*, **82**, 171 (1987).

28 T. DICICCIO and B. EFRON, “Bootstrap Confidence Intervals,” *Statistical Science*, **11**, 189–228 (1996).

29 S. OSHER and R. FEDKIW, *Level Set Methods and Dynamic Implicit Surfaces*, Springer, New York, NY (2003).

30 E. OLSSON and G. KREISS, “A conservative level set method for two phase flow,” *Journal of Computational Physics*, **210**, *1*, 225–246 (2005).

31 E. OLSSON et al., “A conservative level set method for two phase flow II,” *Journal of Computational Physics*, **225**, *1*, 785–807 (2007).

32 M. SANO and K. TAMAI, “A Universal Transition to Turbulence in Channel Flow,” *Nature Physics*, **12**, 249–253 (2016).

33 H. C. JI and R. A. GARDNER, “Numerical analysis of turbulent pipe flow in a transverse magnetic field,” *International Journal of Heat and Mass Transfer*, **40**, 1839–1851 (1997).

34 S. KENJERES and K. HANJALI, “On the implementation of effects of Lorentz force in turbulence closure models,” *International Journal of Heat and Fluid Flow*, **21**, 329–337 (2000).

35 Z. MENG et al., “A K-Epsilon RANS turbulence model for incompressible MHD flow at high Hartmann number in fusion liquid metal blankets,” *International Journal of Energy Research*, **42**, 314–320 (2018).

36 S. SMOLENTSEV et al., Application of the K-epsilon model to open channel flows in a magnetic field, Int. J. Eng. Sci. 40, 693-711 (2002).

37 P. J. ROACHE et al., “Editorial Policy Statement on the Control of Numerical Accuracy,” *ASME Journal of Fluids Engineering*, **108**, *1*, 2 (1986).

38 I. B. CELIK et al., “Procedure for Estimation and Reporting of Uncertainty Due to Discretization in CFD Applications,” *Journal of Fluids Engineering*, **130**, *7*, 078001-078001-4 (2008).

39 M. CASEY and T. WINTERGERSTE, *Best practice guidelines*, ERCOFTAC, Lausanne, CH (2000).

40 S. W. CHURCILL, “Friction-factor equation spans all fluid-flow regimes,” *Chemical Engineering*, **84**, 91–92 (1977).

List of figures captions

List of tables titles